



HAL
open science

Modelling rainfall-induced mudflows using FEMLIP and a unified hydro-elasto-plastic model with solid-fluid transition

Z.H. Li, Frédéric Dufour, Félix Darve

► **To cite this version:**

Z.H. Li, Frédéric Dufour, Félix Darve. Modelling rainfall-induced mudflows using FEMLIP and a unified hydro-elasto-plastic model with solid-fluid transition. *European Journal of Environmental and Civil Engineering*, 2016, 22 (4), pp.491-521. 10.1080/19648189.2016.1210032 . hal-02015641

HAL Id: hal-02015641

<https://hal.science/hal-02015641>

Submitted on 27 Apr 2023

HAL is a multi-disciplinary open access archive for the deposit and dissemination of scientific research documents, whether they are published or not. The documents may come from teaching and research institutions in France or abroad, or from public or private research centers.

L'archive ouverte pluridisciplinaire **HAL**, est destinée au dépôt et à la diffusion de documents scientifiques de niveau recherche, publiés ou non, émanant des établissements d'enseignement et de recherche français ou étrangers, des laboratoires publics ou privés.



Distributed under a Creative Commons Attribution - NonCommercial 4.0 International License

Modelling rainfall-induced mudflows using FEMLIP and a unified hydro-elasto-plastic model with solid-fluid transition

Z.H. Li, F. Dufour* and F. Darve

Grenoble CNRS, UMR 5521, 3SR, Grenoble Alpes University, Grenoble, France

The paper describes a proposed unified hydro-elasto-plastic model with a solid–fluid transition. The model associates a hydro-elasto-plastic model for partially saturated geomaterials, a Bingham’s viscous law, and the transition criterion between solid and fluid states. The model describes both solid and fluid behaviours of partially saturated geomaterials in a unified framework. In addition, this paper describes a novel Finite Element Method with Lagrangian Integration Points (FEMLIP) formulation for solving hydro-mechanical problems. Based on the equilibrium equation of momentum and the continuity equation of water flow, the formulation was developed and implemented in a FEMLIP tool. Bishop’s effective stress expression and proper water retention diagrams were taken into account. A heuristic column and real rainfall-induced mudflows were also simulated and analysed in this study. The permeability effects of partially saturated soil and the effective cohesion were considered, which included consideration of the entire mudflow process. The results were proven satisfactorily in a qualitative fashion.

Keywords: mudflow; hydro-mechanical coupling; solid–fluid transition; partially saturated soil; rainfall-induced slope; permeability; failure; FEMLIP

1. Introduction

Flow-type landslides are a common phenomenon worldwide. They can be attributed to a number of factors, including geology, topography, vegetation, climatic variation and human activities. However, it is well known that landslides occur frequently after intense rainfalls in tropical and temperate regions, especially shallow landslides (Petley, 2012). During wetting (rainfall infiltration) of an unsaturated soil, the increased degree of saturation and decreased suction subsequently decrease the shear strength of the soil. Landslides are frequently very dangerous because of their rapid velocities and long run-out distances. For example, the landslide in Brienz (Switzerland, August 2005) and the mudslide in Gansu (China, August 2010), resulted in more than 1479 fatalities. Development of a numerical tool to analyse and predict landslides is increasingly necessary.

Different failure mechanisms before and after the event challenge the analysis of landslides. A series of questions remain open in international discussions. In this study, we considered only landslides that translate into torrential flows. In general, partially saturated geomaterials exhibit an elasto-plastic solid behaviour that can be described using previously developed elasto-plastic models (Gallipoli, Gens, Sharma, & Vaunat,

*Corresponding author. Email: frederic.dufour@3sr-grenoble.fr

2003; Sheng, Sloan, & Gens, 2004; Wheeler, Sharma, & Buisson, 2003). However, they can also exhibit a fluid-like behaviour with a burst of kinetic energy in the post-failure stage, for saturated and loose cases. At the microscopic level, a landslide can be explained by a ‘weak’ contact network of soil grains in which shear strains develop and the deviatoric stress cannot be supported. Fine soils act as a fluidizer among soil grains. To simulate the entire flow landslide process in a partially saturated soil, a unified solid–fluid model incorporating a hydro-mechanical coupling and a solid–fluid transition can be established. This model can describe both the solid-like behaviour of partially saturated soil in the pre-failure phase using an elasto-plastic model, and the fluid-like behaviour in the post-failure phase using a viscous law. A criterion between the two phases determines the failure of partially saturated soils. Such a unified model is detailed in (Li, Dufour, & Darve, 2016).

Current numerical methods do not adequately describe both these behaviours within the same framework. Numerous mathematical methods analyse a landslide phenomenon as two separate phases (Alonso, Gens, & Delahaye, 2003; Au, 1998; Chen, Dadson, & Chi, 2006; Nakata, Liu, Hyodo, Yoshimoto, & Kato, 2010). Modelling of the elasto-plastic state prior to failure is generally accomplished using the Lagrangian finite element method, which allows for inclusion of historical variables. However, this method is limited when analysing large deformations because of element distortion. Comparatively, the post-failure behaviour of geomaterials is generally simulated using the Eulerian finite element methods with material velocities. These methods are capable of addressing run-out behaviour in large-scale terrains, but do not adequately describe geomaterials in the solid state for tracking elasto-plastic variables. Depth average models have also been used to simulate post-failure behaviour and the propagation phase of a flow landslide (Pastor et al., 2015); however, this type of approach cannot simulate dissipative materials.

The complexity of landslides when considering fully coupled hydro-mechanical behaviour in partially saturated geomaterials requires an adaptable numerical method that is capable of capturing all behaviours, particularly for large deformation processes. To fulfil this need, several particle-based methods have been developed for which a computational grid may be used to speed up the resolution. Because this grid carries no material properties, these methods are classified as mesh-less or mesh-free methods. The Particle Finite Element Method (Zhang, Krabbenhoft, Sheng, & Li, 2015) is a mesh-less method involving a mesh-less finite element interpolation. The mesh is used to discretise the studied domain and to integrate governing equations in a Lagrangian manner. The nodes contain information regarding the global displacement and the physical properties of the materials. Large deformations can be modelled by means of this method, but the required re-meshing at each time step is costly.

Smooth particle hydrodynamics (SPH) (Cascini, Cuomo, Pastor, Sorbino, & Piciullo, 2014) is a well-known technique in which the studied domain is discretised into particles that have a spatial distance or so-called smoothing length. Within this distance, material properties are “smoothed” using a kernel function. Because of its formulation, SPH can be adapted for problems that are dynamically driven and that require a specific solution in the treatment of boundary conditions. In addition, the material point method (MPM) combines the capacities of the Eulerian and Lagrangian methods. The domain is first discretised into a series of mobile particles, Newton’s second law is then solved to determine global displacement in the fixed mesh. While this method is frequently used to describe landslides (Abe, Soga, & Bandara, 2014; Bandara, Ferrari,

& Laloui, 2016; Soga, Alonso, Yerro, Kumar, & Bandara, 2015), it suffers from several weaknesses:

- (1) The linear shape functions frequently induce numerical noises in large displacements cases, when material points cross the background mesh (Abe et al., 2014; Bardenhagen & Kober, 2004). While the Generalised Interpolation Material Point Method has ameliorated this issue, a very fine mesh can still reveal this problem (Abe et al., 2014).
- (2) The numerical weight of the material particles reflects the particle's representative volume which is updated according to the continuum transformation. However, this volume update does not account for the number of particles in a cell. Furthermore, Beuth, Wiecekowsky, and Vermeer (2011) proposed a new version based on a re-computation of the numerical weight, such as the cell weight when constant in time. It should be pointed out that this contribution was first proposed by Moresi et al. (Moresi & Solomatov, 1995) in 1995.
- (3) Higher dimensional shape functions demand additional computational time.

In addition to providing the macroscopic description of the entire landslide process, discrete element methods are also suitable for micromechanical investigation, but computational costs are high. If macroscopic laws are introduced, use of continuous methods is more efficient as long as the flow does not exhibit any discontinuities. After careful consideration, the finite element method with Lagrangian integration points (FEM-LIP), developed from the Particle-in-Cell method (Dufour, 2002; Harlow, 1964; Moresi, Dufour, & Mühlhaus, 2002, 2003), was selected as the preferred numerical method in this study. This method is capable of tracking internal variables and solving large displacements (Dufour, 2002; Dufour & Pijaudier-Cabot, 2005; Moresi et al., 2002, 2003; Prime, Dufour, & Darve, 2013, 2014). In contrast to the MPM, the numerical weight of the material particles used in this method is refreshed at each time step, resulting in an acceptable price of calculation, due to the use of an implicit solver.

The objective of this paper is essentially to validate the proposed unified model with a solid–fluid transition by comparing and analysing its results qualitatively in different cases. The paper is organised as follows. Section 2 presents the unified hydro-elasto-plastic model with a solid–fluid transition for partially saturated geomaterials. The hydro-mechanical coupling in a partially saturated porous media is taken into account, by means of an effective stress with a new formulation of parameter χ , and a hydraulic model that relates water content and suction. Section 3 is devoted to establishing a new FEM-LIP formulation for solving hydro-mechanical problems. Problems induced by the new formulation will be discussed and some possible solutions will be proposed. Moreover, a new solver based on the bi-conjugate gradient stabilised method (BiCGSTAB) is implemented to inverse the non-symmetric matrix. Section 4 presents the modelling of a heuristic partially saturated column. The influences of permeability and effective cohesion on the occurrence time of the failure in a solid state, and the effects of viscosity on flow range in a fluid state are presented. Finally, a real rainfall-induced slope is simulated and analysed. In Section 5, several conclusions and future research prospects are discussed.

2. Unified hydro-elasto-plastic model with a solid–fluid transition for partially saturated geomaterials

For landslides induced by rainfall, especially mudflows, fine soils exhibit a solid-like behaviour in the pre-failure stage and a fluid-like behaviour following a viscous law in the post-failure stage. Proposed unified model, incorporating the behaviours of partially saturated soils during this transitive evolution, was developed during this study, based on work performed by Li et al. (2016). As shown in Figure 1, a global three-dimensional model can be displayed in a one-dimensional form to illustrate the model's intrinsic characteristics. In Figure 1, the ' d^2W ' is the second-order work.

According to the above scheme, a porous saturated to partially saturated medium is described by an elasto-plastic model. Hydro-mechanical coupling is considered by introducing an effective stress and a water retention behaviour in the elasto-plastic model. Using Hill's second-order work expressed as effective stress and the yield stress of a viscous law, the failure condition is assessed for appropriate stress levels. Once failure occurs, the medium exhibits fluid behaviour and large displacements appear. Note that the proposed unified model can be applied for both localised and diffuse modes of failure. However, to avoid any mesh-dependency issues, only the diffuse mode of failure was analysed in this study. For the post-failure regime, the medium is described by a visco-plastic law such as Bingham's law. The plasticity and coupled hydraulic parameters have no physical significance in the fluid form, which is considered as a single unique phase material, as mudflows are observed *in situ*.

2.1. Elasto-plastic model with a hydro-mechanical coupling

2.1.1. Bishop's effective stress

Discussions regarding the selection of appropriate stress variables in partially saturated soils are ongoing and detailed in (Harlow, 1964; Zhang et al., 2015). In this study, the proposed unified model was made applicable for a partially saturated domain (Petley, 2012), using Bishop's effective stress (Bishop, 1959) as follows:

$$\boldsymbol{\sigma}' = \boldsymbol{\sigma} - u_a \mathbf{m} + \chi(u_a - u_w) \mathbf{m} \quad (1)$$

where $\boldsymbol{\sigma}'$, $\boldsymbol{\sigma}$, u_a and u_w are, respectively, the effective stress vector, the total stress vector, the isotropic air pressure and the isotropic water pressure. χ is the Bishop's parameter taken as a scalar in this model, and $\mathbf{m}^T = (1, 1, 1, 0, 0, 0)$ $s = u_a - u_w$ is the suction value. Although recent studies of partially saturated idealised granular media

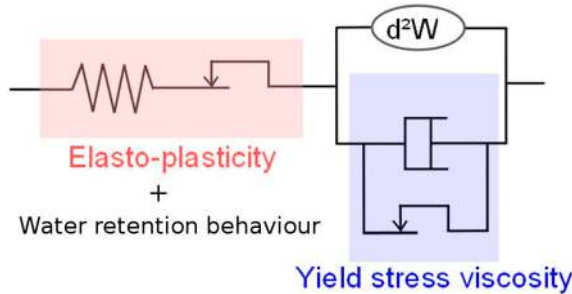


Figure 1. Diagram of the 3D global constitutive model in a 1D general scheme.

have shown the tensorial nature of χ (Scholtès, Chareyre, Nicot, & Darve, 2009; Scholtès, Hicher, Nicot, Chareyre, & Darve, 2009), Bishop's parameter was taken as a scalar for this model to represent a realistic porous media. Bishop's parameter is commonly expressed as $\chi = Sr$; where Sr is the degree of saturation (Bishop, 1959), but this still reflects an idealised media rather than on realistic porous media. Based on the work of Alonso, Pereira, Vaunat, and Olivella (2010), a new formulation of χ determined by two parameters, a_χ and n_χ , was used in this study because of its ability to explain collapse during the wetting process (Arairo, Prunier, Djéran-Maigre, & Darve, 2013). The new formulation of χ is written as follows:

$$\chi = \left(1 + \left(\frac{a_\chi s}{P_{\text{atm}}} \right)^{n_\chi} \right)^{\frac{1}{n_\chi} - 1} \quad (2)$$

where s is the suction value and P_{atm} is the atmospheric pressure. Through proper determination of a_χ and n_χ , the χ formulation can predict many features of partially saturated soil, such as settlement during the wetting path. The determination of a_χ and n_χ must satisfy the requirement specified by (Alonso et al., 2010), χ is considered equivalent to an effective degree of saturation Sr^e that is lower than the main drying curve. Additionally, the value of χ must remain higher than the main wetting curve in the meantime, according to assumptions by (Arairo et al., 2013).

2.1.2. PLASOL elasto-plastic model

A non-associated elasto-plastic model, PLASOL (Barnichon, 1998), can be used with Bishop's effective stress to describe the behaviour of partially saturated geomaterials in the solid stage. The plastic limit of this model is the Van Eekelen plasticity criterion (Van Eekelen, 1980), which is similar to the Mohr–Coulomb plasticity criterion but avoids geometrical singularities. The plasticity criterion is written as follows:

$$f = J_{2\sigma} + m \left(J_{1\sigma'} - \frac{3c}{\tan\phi_c} \right) = 0 \quad (3)$$

where $J_{1\sigma'} = \text{tr}(\boldsymbol{\sigma}')$, $J_{2\sigma} = \sqrt{\text{tr}(\boldsymbol{\tau}^2)}$, $J_{3\sigma} = \sqrt[3]{\text{tr}(\boldsymbol{\tau}^3)}$, ($\boldsymbol{\tau} = \boldsymbol{\sigma}' - \frac{1}{3}\text{tr}(\boldsymbol{\sigma}')\mathbf{I}$) are the three effective stress tensor invariants. \mathbf{I} is the identity matrix, c is the cohesion, ϕ_c is the mobilised friction angle under triaxial compression paths and m is a coefficient defined as follows:

$$m = a(1 + b \sin(3\beta))^n \quad (4)$$

where β is the Lode angle expressed by $\cos 3\beta = \sqrt{6} \left(\frac{J_{3\sigma}}{J_{2\sigma}} \right)^3$, a and b are parameters stated by:

$$a = \frac{r_c}{(1+b)^n}, \quad b = \frac{\left(\frac{r_c}{r_e} \right)^{\frac{1}{n}} - 1}{\left(\frac{r_c}{r_e} \right)^{\frac{1}{n}} + 1} \quad (5)$$

where n is an exponent intended to control the shape of the yield surface, whose default value is -0.299 according to Van Eekelen's suggestion (Van Eekelen, 1980). The parameters, r_c and r_e are the reduced radii for compression and extension of the triaxial tests, respectively, and are calculated as follows:

$$r_c = \frac{1}{\sqrt{3}} \left(\frac{2 - \sin\varphi_c}{3 - \sin\varphi_c} \right), \quad r_e = \frac{1}{\sqrt{3}} \left(\frac{2\sin\varphi_e}{3 + \sin\varphi_e} \right) \quad (6)$$

where φ_e is the mobilised friction angle under triaxial extension paths.

The PLASOL model can also be used to simulate hardening of the yield surface during loading. By introducing the Von Mises equivalent plastic strain, $\mathbf{E}_{eq}^p = \sqrt{\frac{2}{3}} \mathbf{e}_{ij}^p \mathbf{e}_{ij}^p$, ($\mathbf{e}^p = \boldsymbol{\varepsilon}^p - \frac{1}{3} \text{tr}(\boldsymbol{\varepsilon}^p) \mathbf{I}$, the compression, extension friction angles and the cohesion, which are formulated in Equation (7), vary between elastic initial values ($c_0, \varphi_{e0}, \varphi_{c0}$) and plastic limit values ($c_f, \varphi_{ef}, \varphi_{cf}$) during the plastic regime.

$$\begin{aligned} \varphi_c &= \varphi_{c0} + \frac{(\varphi_{cf} - \varphi_{c0}) \mathbf{E}_{eq}^p}{B_p + \mathbf{E}_{eq}^p} \\ \varphi_e &= \varphi_{e0} + \frac{(\varphi_{ef} - \varphi_{e0}) \mathbf{E}_{eq}^p}{B_p + \mathbf{E}_{eq}^p} \\ c &= c_0 + \frac{(c_f - c_0) \mathbf{E}_{eq}^p}{B_c + \mathbf{E}_{eq}^p} \end{aligned} \quad (7)$$

where B_c and B_p are hardening parameters corresponding to the values of \mathbf{E}_{eq}^p for which half of the hardening on friction angles and cohesion is reached.

Lastly, a non-associated plastic law, differing from \mathbf{f} , is formulated as follows:

$$g = J_{2\sigma} + m' \left(J_{1\sigma'} - \frac{3c}{\tan\varphi_c} \right) \quad (8)$$

where m' retains the same form as m , but dilatation angles, ψ_c in compression and ψ_e in extension are substituted for ϕ_c and ϕ_e . Taylor's rule $\psi_{cf} - \psi_c = \varphi_{cf} - \varphi_c$ is followed to define the dilatation angles (Taylor, 1948). Consequently, only one ψ value is needed.

In total, 13 parameters are required to adequately describe the elasto-plastic behaviour of soils:

E, ν : Young's modulus and Poisson's coefficient

$\varphi_{c0}, \varphi_{cf}$: mobilised friction angles at elastic and plastic limits under triaxial compression

$\varphi_{e0}, \varphi_{ef}$: mobilised friction angles at elastic and plastic limits under the triaxial extension

ψ_c, ψ_e : dilatation angles under triaxial compression and extension

c_0, c_f : cohesions at elastic and plastic limits

B_c, B_p : hardening parameters

n : exponent to control yield surface shape

2.1.3. Water retention behaviour

By relating degree of saturation and suction, water retention curves (WRC) can be used to describe the hydro-mechanical properties of partially saturated soil. As shown in Figure 2, complete hydraulic model generally includes a boundary drying curve, a wetting curve and two types of scanning curves. The degree of saturation is generally greater in the drying process than in the wetting process for a given suction, resulting in a hydraulic hysteresis.

Numerous hydraulic models have been previously proposed (Feng & Fredlund, 1999; Fredlund & Xing, 1994; Mualem, 1974; Parlange, 1980; Van Genuchten, 1980). The modified Van Genuchten–Mualem model was selected for our work, because its boundary curves are commonly used and its scanning curves are simple and precise.

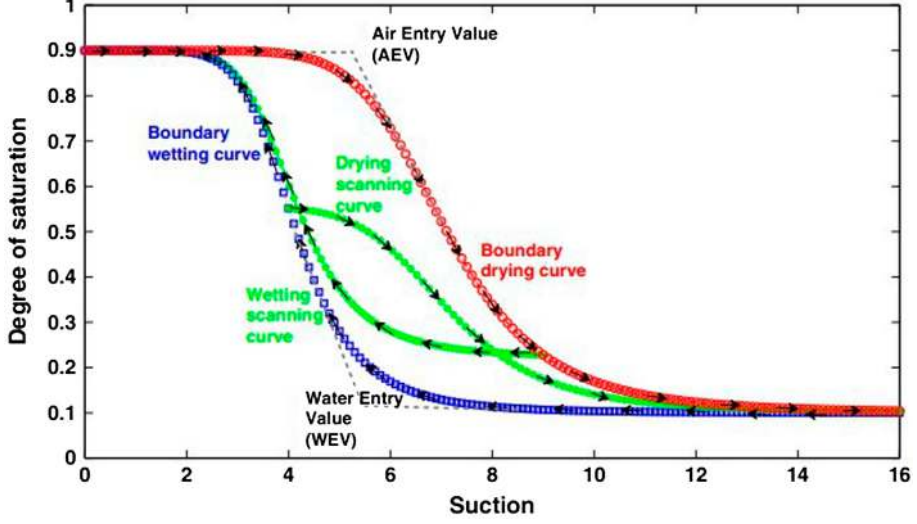


Figure 2. Scheme of water retention curves for partially saturated soil.

The modified Van Genuchten–Mualem model with a hydraulic hysteresis, taking into account the relationship between the degree of saturation and porosity (Arairo et al., 2013), was used to complete the hydro-mechanical coupling. The model formulation is as follows:

$$Sr_v = Sr_{res} + (Sr_{sat} - Sr_{res}) \left(1 + \left(\frac{a_v s}{P_{atm}} \right)^{n_v} \right)^{\frac{1}{n_v} - 1} \quad (9)$$

where the index v stands for d or w respectively for the drying or wetting processes, Sr_{res} , Sr_{sat} and Sr_v are, respectively, the residual, saturated and current degrees of saturation, a_v and n_v are two parameters. The former is expressed as follows (Arairo et al., 2013):

$$a_v = \frac{P_{atm}}{s_{aev}} \left(\frac{n_v - 1}{n_v} \right)^{\frac{1}{n_v}} \frac{-n_v}{(n_v - 1)^2} \left(\left(\frac{2n_v - 1}{n_v} \right)^{2 - \frac{1}{n_v}} - \left(\frac{2n_v - 1}{n_v} \right) - \frac{(n_v - 1)^2}{n_v} \right) \quad (10a)$$

where s_{aev} is the air entry value (AEV) that is dependent on n and is determined as follows: (Arairo et al., 2013):

$$s_{aev} = s_{aev0} \exp \left(\lambda \left(\frac{1}{n} - \frac{1}{n_0} \right) \right) \quad (10b)$$

where s_{aev0} is the reference AEV for a reference porosity n_0 and λ is a material parameter. Thus, the hydro-mechanical model is dependent on not only suction but also porosity.

The hydro-mechanical model also includes two scanning curve equations as follows:

$$Sr_d(s_1, s) = Sr_w(s) + \frac{Sr_w(s_1) - Sr_w(s)}{Sr_{sat} - Sr_w(s)} (Sr_d(s) - Sr_w(s)) + \Delta Sr_1 \quad (11a)$$

$$\text{Sr}_w(s_2, s) = \text{Sr}_w(s) + \frac{\text{Sr}_{\text{sat}} - \text{Sr}_w(s)}{\text{Sr}_{\text{sat}} - \text{Sr}_w(s_2)} (\text{Sr}_d(s_2) - \text{Sr}_w(s_2)) + \Delta\text{Sr}_2 \quad (11b)$$

where $\text{Sr}_w(s)$ and $\text{Sr}_d(s)$ are the degrees of saturation on the boundary wetting and drying curves, respectively, for a suction value s . s_1 and s_2 are the suction values on the boundary wetting curve from which the scanning drying curve starts, and on the boundary drying curve from which the scanning wetting curve starts, respectively. The differences between the two calculated degrees of saturation are given as $\Delta\text{Sr}_1 = \text{Sr}_d(s_1, \hat{s}) - \text{Sr}_w(s_1, \hat{s})$ and $\Delta\text{Sr}_2 = \text{Sr}_d(s_2, \hat{s}) - \text{Sr}_w(s_2, \hat{s})$, where \hat{s} is the current suction value when the cycle is reversed (from wetting to drying or from drying to wetting). Note that either ΔSr_1 or ΔSr_2 will be zero for the first reversal of the cycle (Arairo et al., 2013).

2.2. Solid–fluid transition criterion

Geomaterials are notably non-associated materials regarding the bifurcation domain of failures. As defined, bifurcation can cause a sudden or discontinuous change in the response mode while a constant or infinitesimal perturbed load is charged (Prunier, Laouafa, Lignon, & Darve, 2009). A typical example of bifurcation in the geomaterial domain is the liquefaction of loose sand during an undrained triaxial compression test (Khoa, Georgopoulos, Darve, & Laouafa, 2006). The bifurcation domain is delimited by a plasticity criterion corresponding to the disappearance of the determinant of \mathbf{M} at the upper limit, and by the second-order work criterion corresponding to the disappearance of $\det \mathbf{M}_s$ at the lower limit. \mathbf{M} is the constitutive matrix and \mathbf{M}_s is the symmetric part of \mathbf{M} . For associated materials, \mathbf{M} is symmetric and the disappearance of $\det \mathbf{M}$ and $\det \mathbf{M}_s$ are equivalent. However, for non-associated materials \mathbf{M} is not symmetric. Additionally, according to linear algebra principles, $\det \mathbf{M}_s$ will vanish before $\det \mathbf{M}$ (Laouafa, Prunier, Daouadji, Al Gali, & Darve, 2011). Thus, the bifurcation is considered once the second-order work criterion is met.

At the lower limit of the bifurcation domain, the second-order work criterion is considered the most conservative criterion and can be used to determine the potential instability of geomaterials (Darve, Servant, Laouafa, & Khoa, 2004; Khoa et al., 2006; Laouafa et al., 2011; Nicot, Dauuadji, Laouafa, & Darve, 2010; Prunier et al., 2009). This criterion was selected for use in this study to determine the solid–fluid transition for the unified model. The second-order criterion is formulated as follows:

$$d^2w = d\boldsymbol{\sigma}'_ij d\boldsymbol{\varepsilon}_{ij} \quad (12a)$$

where $\boldsymbol{\sigma}'$ and $\boldsymbol{\varepsilon}$ are the effective stress and the strain tensors, respectively. The second-order work written by the effective stress is used, since the instabilities of the granular skeleton are of interest. If $d^2w > 0$ for all loading directions, the material is considered stable. Otherwise, diffuse or localised failures can occur in the directions for which the values are negative. To maintain reasonable computational time in this study, the second-order work criterion in Equation (12b) was only calculated for the loading direction.

The second-order work expressed as Equation (12a) was calculated locally for each material points in the domain. To analyse the boundary value problem where geometry, initial and boundary conditions are taken into account, the global second-order work can be normalised and formulated (Khoa, 2005) as follows:

$$D^2W = \frac{\sum(d^2w_i \cdot w_i J_i)}{(\sum w_i J_i)(\sum \|d\sigma'_i\| \|d\epsilon_i\|)} \quad (12b)$$

where w_i is the numerical weight of the integration point i and J_i is the determinant of the Jacobian matrix. Equation (12b) can be used to globally determine whether an entire soil mass behaves as a solid or fluid.

2.3. Bingham's viscous law

Geomaterials can be considered as viscous fluid using Bingham's yield stress s_y in the post-failure stage (Coussot, Proust, & Ancey, 1996; Daido, 1971). By neglecting the non-linearity of the viscous relationship and the dependency of the yield stress on confinement, geomaterials can be described by the simplified Bingham's viscous law. Considering prior formulation by Duvaut and Lions (1972) and Balmforth and Craster (1999), the simplified Bingham's viscous law for three dimensions is as follows:

$$\text{If : } J_{2\sigma} > s_y \quad \dot{\epsilon}_{ij} = \frac{1}{2\eta} \left(\tau_{ij} - s_y \frac{\tau_{ij}}{J_{2\sigma}} \right) = \frac{J_{2\sigma} - s_y}{2\eta} \cdot \frac{\tau_{ij}}{J_{2\sigma}} \quad \text{else : } \dot{\epsilon}_{ij} = 0 \quad (13)$$

where $J_{2\sigma}$ is the second stress tensor invariant, τ and $\dot{\epsilon}$ are the deviatoric stress and strain rate tensors, respectively. η is the dynamic viscosity. When $d^2w < 0$ and $J_{2\sigma} > s_y$ are both satisfied, a solid–fluid transition occurs. Note that for initially partially saturated soil, suction effects disappear once failure occurs in the studied medium, since the mud is considered as a viscous monophasic fluid. Therefore, distinguishing total stress and effective stress in the fluid stage is meaningless. In the fluid state, when $J_{2\sigma} < s_y$, the material returns to a solid state (from a fluid state) following elasto-plastic behaviour. However, in the proposed model, we were not interested in the detailed elasto-plastic behaviour following failure. Thus, the elasto-plastic parameters were assumed constant for the pre-failure and post-failure stages (although they would obviously be different).

To summarise, the proposed hydro-elasto-plastic unified model with a solid–fluid transition involves multiple steps: The saturated or partially saturated porous medium is first described by the PLASOL elasto-plastic model. The use of Bishop's effective stress and the modified Van Genuchten–Mualem's hydraulic model accounts for the hydro-mechanical coupling in the solid stage. Failure occurs along the loading path, once the second-order work criterion expressed in effective stress is met. The medium flows in large displacements, obeying Bingham's viscous law (Bingham's yield stress criterion is required to be met).

As illustrated in Figure 3, Bingham's yield stress is generally lower than Van Eekelen elastic's limit, and the second-order work vanishes only in the elasto-plastic domain (Li et al., 2016). In addition, when $J_{2\sigma} < s_y$ in the fluid state, the medium returns to a solid state (from a fluid state) and exhibits renewed elasto-plastic behaviour. During a mudflow, the flow stops and the mud begins to once again sedimentate. The debate regarding the physical explanation of the mudflow is still an ongoing subject of discussion. Experience indicates that a monophasic fluid no longer possesses an organised microstructure because of destructive forces during the mudflow. For all fluid types considered by Bingham, materials return to solid if the deviatoric stress is not sufficiently large. A gently sloped terrain can contribute to a reduction in deviatoric stress.

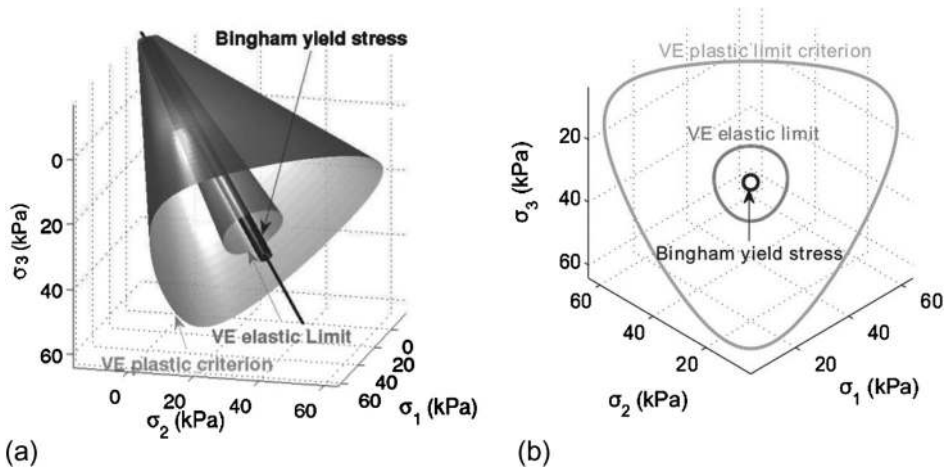


Figure 3. Unified model in the principal stress space ('VE' means Van Eekelen) (a) 3D view and (b) deviatoric stress plane view.

3. A new FEMLIP model for solving hydro-mechanical problems

A simulation model that comprehensively describes the solid–fluid behaviours of geomaterials must include the following three capacities:

- *Internal variables trackings.* Landslides comprise geomaterials with an elasto-plastic behaviour in their solid-like phase. Internal variables associated with the material points (i.e. hardening parameters and plastic strains) must be tracked in time and space to calculate plasticity, which is an intrinsic function of the load history.
- *Strict pursuit of the materials in space.* Simulation involves different materials, their interactions, their spatial movements and the demand to strictly identify the materials positions over time.
- *Large displacement solutions.* Landslides, especially mudflows, require not only small transformations in a solid state, but also large displacements as the geomaterials spread over long distances in their fluid state.

The elasto-plastic behaviour of partially saturated soils with infiltration process included as well as the fluid behaviour following failure has been previously modelled by several researchers (Alonso et al., 2003; Au, 1998; Chen et al., 2006; Nakata et al., 2010). However, it is difficult to solve large displacements using classical finite element methods, excessive element distortions preclude integration of a volume or surface using the Lagrangian finite element methods. Alternatively, it is difficult to track the elasto-plastic models without diffusion within the framework of the Eulerian finite element methods.

To satisfy the three simulation model capacities described above, the FEMLIP was chosen for simulation in this study. As illustrated in Figure 4(a, b), the computational domain is discretised by means of a computational Eulerian grid while the material distribution is spatially discretised using Lagrangian material points. The grid is fixed and used to obtain the nodal equations. With the material kinematic field solved according to equilibrium equations, each material point moves between time t and $t + \Delta t$ as

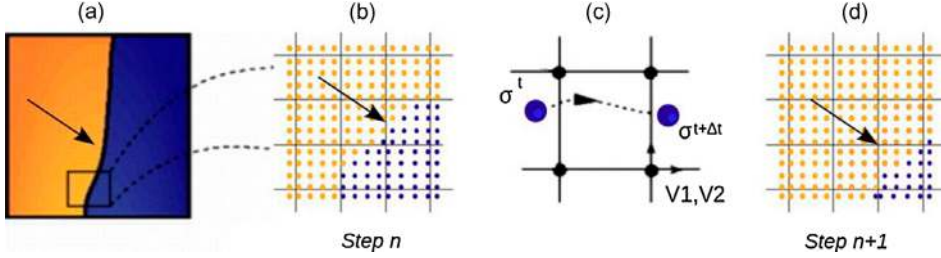


Figure 4 (a-d). Calculation process of FEM-LIP.

illustrated in Figure 4(c). At the end of the incremental calculation, the configuration is updated to reflect the new position of the material points, as illustrated in Figure 4(d). It should be noted that the material points follow the integration points rule. Because the Gaussian quadrature is verified for the numerical weight computation, a computational cell cannot be empty of a particle. Thus, for the free surface simulation, the empty volume must be filled with particles possessing negligible mechanical properties, such as air particles.

For computational efficiency, a multi-grid scheme was used in this study. This method is most efficient when used with regular mesh. Developed initially for solving incompressible fluid problems, regular quadrangle elements with bi-linear interpolation for the velocity field and constant interpolation for the pseudo-pressure field were chosen, to satisfy the Ladyzansky-Babuska-Brezzi stability condition and prevent locking problems (Dufour, 2002; Hughes, 1987). The quadrangle elements with bi-linear interpolation and constant interpolation were used to calculate the velocity and the water pressure fields, respectively. This information was subsequently transferred to the material points, according to corresponding shape functions. Lastly, the elasto-plastic and hydraulic variables were calculated and stored in the material points. To ensure calculation accuracy, the numerical weights of the integration points were refreshed to reflect position and the number of material points in each element (this step differs from the previously described MPM).

3.1. Control equations

Deformable partially saturated porous geomaterials are widely considered a three-phase mixed medium, comprising solid, liquid and gas phases and soil skeleton, water, vapour and air constituents. To solve multi-phase material problems, mechanical variables for each phase that reveal constitutive relationships should be defined. This relationship should consider between phases interaction laws, conservation laws, equilibrium equations and the energy balance. To simplify the system of equations, several assumptions were made in this study:

- (1) Densities of solid grains and liquid were assumed constant. Therefore, the liquid and solid phases were incompressible.
- (2) Liquid flows obeyed the generalised Darcy's law in the connected voids of the medium.
- (3) Gas diffusion was negligible under atmospheric air pressure; the pressure of air and water vapour were considered nil (i.e. pores connected to the outside air).

- (4) Heat transfer was negligible under isothermal conditions, and the temperature field was assumed to be constant.

As a result, the control equations consisted of the momentum equilibrium equation for the whole body and the continuity equation for water flow. The weak form of the equilibrium equation is expressed as follows:

$$\int_V (\partial \boldsymbol{\varepsilon}^T \boldsymbol{\sigma}) dV - \int_S (\partial \mathbf{u}^T \mathbf{f}) dS - \int_V (\partial \mathbf{u}^T \mathbf{b}) dV = 0 \quad (14)$$

The latter, which is composed by the conservation equation of water mass and the generalised Darcy's law, is written as follows:

$$\text{div} \left(-\frac{\mathbf{k}}{g} (\nabla \mathbf{u}_w - \mathbf{b}_w) + \frac{\partial}{\partial t} (\rho_w \theta) \right) = 0 \quad (15)$$

where S and V are the boundary values subjected to the distributed force \mathbf{f} and the considered volume, respectively, while $\boldsymbol{\sigma}$ is the Cauchy total stress tensor and \mathbf{b} is the volume force vector. The gravity acceleration is g , ρ_w is the water density, \mathbf{b}_w is the body force vector of pore water, \mathbf{u}_w is the pore water pressure and \mathbf{k} is the permeability matrix for partially saturated soil. In the Equation (14), the inertial term is provisionally neglected in the considered formulation, which may introduce inaccuracies in the simulation of very fast phenomena. However, they will be taken into account in a further development of the study. The inertial effect is significant in many dynamic problems.

3.2. Incremental constitutive relations

To solve hydro-mechanical boundary value problems in an FEM-LIP framework, an understanding of the stress–strain and water content–suction relations are necessary. Because the FEM-LIP model was initially developed based on a visco-elastic framework, the stress–strain relationship can be expressed as: $\Delta \boldsymbol{\sigma} = \mathbf{D}^{ve} \dot{\boldsymbol{\varepsilon}}$ (Dufour, 2002; Moresi et al., 2002, 2003), where $\Delta \boldsymbol{\sigma} = \boldsymbol{\sigma}^{t+\Delta t} - \boldsymbol{\sigma}^t$ and \mathbf{D}^{ve} presents the visco-elastic constitutive tensors. Implementation of the plasticity is performed explicitly based on the visco-elastic matrix (Prime et al., 2013, 2014). By incorporating the hydro-mechanical coupling, Bishop's effective stress in Equation (1) can be rewritten as follows:

$$\bar{\boldsymbol{\sigma}}^{t+\Delta t} = \mathbf{D}^{ve} \dot{\boldsymbol{\varepsilon}}^{t+\Delta t} - (\chi s)^{t+\Delta t} \mathbf{m} + \boldsymbol{\sigma}^t \quad (16)$$

where $\bar{\boldsymbol{\sigma}}^{t+\Delta t}$ is the net stress vector defined as: $\bar{\boldsymbol{\sigma}}^{t+\Delta t}$, $\dot{\boldsymbol{\varepsilon}}^{t+\Delta t}$ is the strain rate vector, $s^{t+\Delta t}$ is the suction. All variables are measured at time t and $t + \Delta t$. To obtain a unified form with the water content–suction relationship, this expression can be rewritten using $s^{t+\Delta t} = \Delta t \cdot \dot{s}^{t+\Delta t} + s^t$, as follows:

$$\bar{\boldsymbol{\sigma}}^{t+\Delta t} = \mathbf{D}^{ve} \dot{\boldsymbol{\varepsilon}}^{t+\Delta t} - \Delta t \chi^t \dot{s}^{t+\Delta t} \mathbf{m} - \chi^t s^t \mathbf{m} + \boldsymbol{\sigma}^t \quad (17)$$

It should be noted that χ is assumed constant for a sufficiently small Δt , for the sake of simplification. Additionally, χ is updated at each time step. As a result, a common stress–strain relationship in the hydro-mechanical visco-elastic framework is derived.

With the water content expressed as $\theta = n \cdot S_r$, the water content–suction relationship can be established using the modified Van Genuchten–Mualem's WRCs in Equation (9) as follows:

$$\begin{aligned}
d\theta &= \text{Sr}dn + n d\text{Sr} = \left(\text{Sr} + \frac{\partial \text{Sr}}{\partial n} \right) dn + n \frac{\partial \text{Sr}}{\partial s} ds \\
&= -(1-n) \left(\text{Sr} + n \frac{\partial \text{Sr}}{\partial n} \right) \mathbf{m}^T d\boldsymbol{\varepsilon} + n \frac{\partial \text{Sr}}{\partial s} ds
\end{aligned} \tag{18}$$

The water content is consequently determined using suction and porosity.

Combining Equations (17) and (18), a matrix relation is derived as follows:

$$\begin{pmatrix} \bar{\boldsymbol{\sigma}}^{t+\Delta t} \\ \dot{\theta}^{t+\Delta t} \end{pmatrix} = \begin{pmatrix} \mathbf{D}^{ve} & \mathbf{W} \\ \mathbf{T} & H \end{pmatrix} \begin{pmatrix} \dot{\boldsymbol{\varepsilon}}^{t+\Delta t} \\ \dot{s}^{t+\Delta t} \end{pmatrix} + \begin{pmatrix} -\chi^t s^t \mathbf{m} + \boldsymbol{\sigma}^t \\ 0 \end{pmatrix} \tag{19}$$

where

$$\mathbf{W} = -\chi^t \mathbf{m} \Delta t$$

$$\mathbf{T} = -(1-n) \left(\text{Sr} + n \frac{\partial \text{Sr}}{\partial n} \right) \mathbf{m}^T$$

$$H = n \frac{\partial \text{Sr}}{\partial s}$$

In Equation (19), \mathbf{W} and \mathbf{T} are a six-element column vector and a six-element row vector, respectively; H is a scalar. According to the modified Van Genuchten–Mualem’s WRCs in Equation (9), $\frac{\partial \text{Sr}}{\partial n}$ and $\frac{\partial \text{Sr}}{\partial s}$ can be determined as follows:

$$\frac{\partial \text{Sr}}{\partial s} = (\text{Sr}_{\text{sat}} - \text{Sr}_{\text{res}}) (1 - n_v) \frac{a_v}{P_{\text{atm}}} \left(1 + \left(\frac{a_v s}{P_{\text{atm}}} \right)^{n_v} \right)^{\frac{1}{n_v} - 2} \left(\frac{a_v s}{P_{\text{atm}}} \right)^{n_v - 1} \tag{20}$$

$$\frac{\partial \text{Sr}}{\partial n} = \lambda (\text{Sr}_{\text{sat}} - \text{Sr}_{\text{res}})$$

$$\left(1 + \left(\frac{a_v s}{P_{\text{atm}}} \right)^{n_v} \right)^{\frac{1}{n_v} - 2} \left(\frac{a_v s}{P_{\text{atm}}} \right)^{n_v - 1} \frac{s}{s_{\text{ae}v}^2} \left(\frac{n_v - 1}{n_v} \right)^{\frac{1}{n_v} - 1} \frac{s_{\text{ae}v0}}{n_0} \left(\frac{2n_v - 1}{n_v} \right)^{2 - \frac{1}{n_v}} - n_v \tag{21}$$

The relationships to be integrated into the FEMLIP framework are now established, with both the strain rate and suction rate appearing on the right side of the equation. Therefore, the velocity and the pore water pressure fields can be solved in the corner nodes and central nodes, respectively. The solution is then transferred to the material points where the strain, stress, and saturation fields are solved locally using the unified model with a solid–fluid transition.

3.3. FEMLIP model formulation

With the linear and constant shape functions \mathbf{N} and N_w , representing the velocity and water pressure fields, respectively, the discrete finite element equation is as follows, based on the control equations and Equation (19):

$$\begin{pmatrix} \mathbf{A} & \mathbf{L} \\ \mathbf{L}^T & \mathbf{S} \end{pmatrix} \begin{pmatrix} \dot{\mathbf{U}}^{t+\Delta t} \\ \dot{\mathbf{U}}_w^{t+\Delta t} \end{pmatrix} + \begin{pmatrix} \mathbf{0} \\ \mathbf{R} \mathbf{U}_w^{t+\Delta t} \end{pmatrix} = \begin{pmatrix} \mathbf{F}^{t+\Delta t} - \mathbf{M} \mathbf{U}_w^t \\ \mathbf{Q}_{\text{ext}}^{t+\Delta t} \end{pmatrix} \tag{22}$$

where

$$\mathbf{A} = \int_V (\mathbf{B}^T \mathbf{D}^{ve} \mathbf{B}) dV$$

$$\mathbf{L} = - \int_V (\mathbf{B}^T \mathbf{W} N_w) dV$$

$$\mathbf{M} = \sum \int_V (\mathbf{B}^T \chi^t \mathbf{m} N_w) dV$$

$$\mathbf{F}^{t+\Delta t} = \sum \left(\int_V (\mathbf{N}^T \mathbf{b}^{t+\Delta t} - \mathbf{B}^T \boldsymbol{\sigma}^t) dV + \int_s (\mathbf{N}^T \mathbf{t}^{t+\Delta t}) dS \right)$$

$$\begin{aligned}
L' &= \sum \int_V (N^T \mathbf{T} \mathbf{B}) dV \\
S &= - \sum \int_V (N_w^T H N_w) dV \\
R &= \sum \int_V (\mathbf{B}_w^T \frac{k}{\rho_w g} \mathbf{B}_w) dV \\
Q_{ext}^{t+\Delta t} &= - \sum \left(\int_{S_w} (N_w^T q^{t+\Delta t}) dS_w - \sum \int_V (\mathbf{B}_w^T \frac{k}{\rho_w g} \mathbf{b}_w) dV \right)
\end{aligned}$$

In these relationships, \mathbf{B} is the gradient matrix of the shape function N , $q = \mathbf{n}^T V_k$, V_k is the infiltration velocity, and \mathbf{n}^T is a unit vector normal to the surface subjected to water flux. Equation (22) is further detailed by (Li et al., 2016).

By introducing $\dot{U}_w^{t+\Delta t} = \frac{U_w^{t+\Delta t} - U_w^t}{\Delta t}$, a system of equations for determining the velocity and the pore water pressure fields can be derived from Equation (22) as follows:

$$\begin{aligned}
A \dot{U}^{t+\Delta t} + \frac{L}{\Delta t} U_w^{t+\Delta t} &= F^{t+\Delta t} \\
L' \dot{U}^{t+\Delta t} + \left(\frac{S}{\Delta t} + R \right) U_w^{t+\Delta t} &= Q_{ext}^{t+\Delta t} + \frac{S}{\Delta t} U_w^t
\end{aligned} \tag{23}$$

This derivation represents the proposed FEMLIP formulation that incorporates hydro-mechanical coupling.

After transformations, Equation (23) can be rewritten as:

$$\widehat{A} U_w^{t+\Delta t} = \widehat{F} \tag{24}$$

where

$$\begin{aligned}
\widehat{A} &= L' A^{-1} \frac{L}{\Delta t} - \left(\frac{S}{\Delta t} + R \right) \\
\widehat{F} &= L' A^{-1} F^{t+\Delta t} - \left(Q_{ext}^{t+\Delta t} + \frac{S}{\Delta t} U_w^t \right)
\end{aligned}$$

To solve Equation (24), which is a linear equation with a non-symmetric matrix \widehat{A} , the BICGSTAB method proposed by Van der Vorst (van der Vorst, 1992) was implanted in the code as a new solver. This method is developed on the basis of the bi-conjugate gradient method (BiCG) and is able to inverse the non-symmetric matrix with sufficiently fast and smooth convergence. Additionally, the multi-grid scheme was used to decrease computational cost.

3.4. FEMLIP model considerations

In complex landslide simulations based on FEMLIP, several material types may coexist such as hydro-elasto-plastic geomaterials that may become viscous, elastic obstacles in concrete and low-viscous air that fills the remaining space. The geomaterials naturally implicate hydro-mechanical coupling; however, other materials (e.g. air) do not physically implicate any hydro-mechanical coupling. For finite elements filled with HM particles (soil) and not HM particles (air) as illustrated in Figure 5, the calculation is frequently disturbed. Water pressure in the central nodes and hydraulic parameters in the corner nodes must be wholly integrated at the start of each incremental calculation. At the end of each incremental calculation, the water pressures will be transferred to all the integration points. Hence, during computation, any non-zero water pressures and other non-physical parameters will be included in the integration. Error accumulates with each time step of the calculation and induces a loss of convergence.

One solution is to classify the material points into two types: (1) non hydro-mechanical and (2) hydro-mechanical. The first classification does not implicate or track

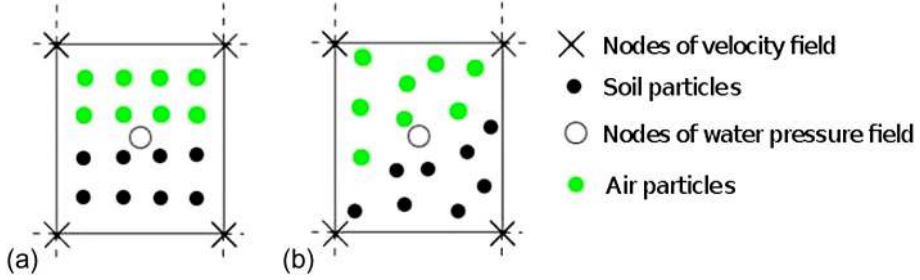


Figure 5 (a, b). Configuration of elements mixed by two types of particles.

hydraulic variables. For these material points, water pressure and all other hydraulic parameters are null during calculation; water pressure transmission between the central nodes and material points is effectively interrupted. The finite element formulation can be expressed as $\mathbf{A}\mathbf{U}=\mathbf{F}$. The second classification implicates hydro-mechanical coupling, in which the water pressures are refreshed and the water content–suction relationship is considered at each time step of the calculation. Note that the water pressure field is smoothed out by first extrapolating the piecewise constant field to the corner nodes and then back to the particles using linear shape functions. Water pressures at the integration points are transmitted using the following equations:

$$\mathbf{u}_w = \mathbf{N}\mathbf{U}_w \quad \text{for hydro – mechanical points} \quad (25a)$$

$$\mathbf{u}_w = 0 \quad \text{for non hydro – mechanical points} \quad (25b)$$

This two-part classification theoretically ensures that the representative water pressure in an element U_w (at the central node) is determined only by the water pressures of soil particles u_w in that element. Hence, the stability of the calculation is assured.

However, this approach can give rise to additional problems. Note that the velocity and the water pressure fields at t are refreshed at the computational nodes based on the configuration at $t - \Delta t$. The velocity and water pressure fields are transferred to each of the integration points to perform the local calculation. The integration of local data, including local water pressures, is performed based on the configuration at $t - \Delta t$. The integration points move according to the solved velocity field and a corresponding configuration at t appears. Thus, the integration of local water pressures is performed before the movement of integration points at each incremental computation. When the integration points (with non-zero water pressures) enter an element completely filled with non hydro-mechanical points (with null water pressures in the central node), an error occurs.

As illustrated in Figure 6(a), the element on the left is completely filled with soils and the one on the right is completely filled with air. Hence, the water pressure of the right element at $t - \Delta t$ is $U_w^{t-\Delta t} = 0$. Figure 6(b) shows that four soil particles moved after calculation at t , but $U_w^t = 0$, because the value was determined completely by the air particles before entry of the soil particles. Consequently, $U_w^{t+\Delta t}$ will be calculated from an initial null value, even though soil particles are present. These calculations can also be influenced by other variables, such as velocity, if no other boundary conditions exist. Because of this, error resolution is not predictable. In any case, the water pressures of entering particles will be undetected. This phenomenon sometimes results in a loss of convergence during the calculation.

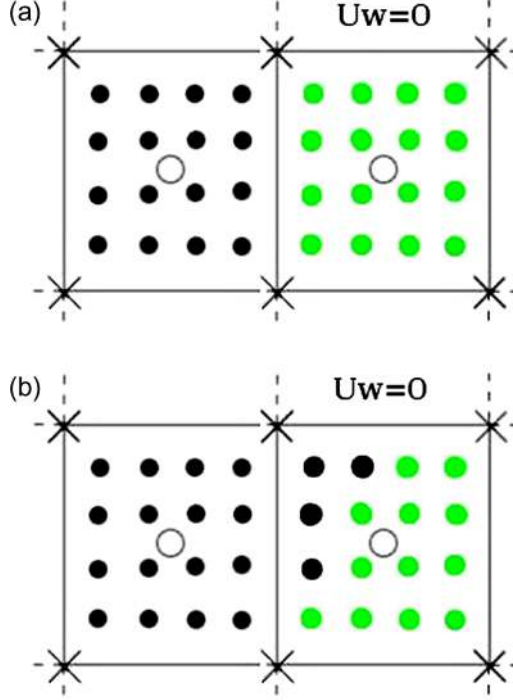


Figure 6 (a, b). Error induced by entry of hydro-mechanical particles into an air element.

To address this problem, the FE tool checks all elements at the end of each incremental calculation. For elements completely filled with dry particles and into which hydro-mechanical particles enter, a re-integration at the central nodes is performed to ensure that the water pressures U_w is effectively controlled by the hydro-mechanical particles. This relationship is as follows:

$$U_w = \frac{\sum_{i=1}^{n_{HM}} u_{wi}}{n_{HM}} \quad (26)$$

where U_w and u_{wi} are the water pressures in the central node and at the integration points, respectively, and n_{HM} is the number of hydro-mechanical particles in an element.

4. FEMLIP simulations and analysis

Mechanical features of partially saturated geomaterials described by the hydro-elasto-plastic unified model were previously validated by Li et al. (2016). In this study, a boundary value problem was simulated to show the potentialities of the unified model in FEMLIP. The effects of partially saturated permeability, effective cohesion and viscosity on the behaviours described by the unified model were assessed, and appeared reasonable; Quantitative comparisons with analytical and experimental solutions will be considered in the future.

In this study, an unsaturated, initially stable, 6×6 m² slope with a homogeneous initial suction of 500 kPa, was simulated. Gravity increased linearly for the first 100 time

steps, until a value of 9.81 was reached m/s^2 . The remaining space was filled with air, a viscous material with a 2000 Pa s pre-failure viscosity and a 20 Pa s post-failure viscosity. It is obviously too large comparing the real case and will certainly influence the results in the post-failure stage, but the ratio of effective viscosity of soil and viscosity of air must be less than 10^3 , in order to void the loss of convergence due to ill-conditioned matrix (Prime, 2012).

The soil was discretised by a series of material points. All boundaries were free slip; the horizontal displacement at the left boundary was constrained while displacement at the right boundary was free. Rainfall on the top surface (lasting 79 h) induced an infiltration from top to bottom under a constant water flux of 1.8 mm/h ($5 \cdot 10^{-7}$ m/s).

In the FEMLIP model, the slope's permeability tensor was assumed isotropic for the sake of simplification, and the permeability of the partially saturated soil k was determined by $k = k_r \cdot k_s$, k_s is the permeability of saturated soil and k_r the relative hydraulic conductivity. In the paper, k_r was determined using relationship previously derived by Van Genuchten (van Genuchten, 1980) as follows:

$$k_r = \frac{\left(1 - (a_v s)^{n_v - 1} (1 + (a_v s)^{n_v})^{\frac{1}{n_v} - 1}\right)^2}{\left(1 + (a_v s)^{n_v}\right)^{\frac{1 - \frac{1}{n_v}}{2}}} \quad (27)$$

4.1 Modelling and analysis of suction and permeability

The parameters used in the simulation are enumerated in Tables 1 and 2:

In Table 2, k_s is the initial permeability of the saturated soil. The permeability of the partially saturated soil, which controls the infiltration capacity, was determined using Equation (27). The gradients of the water pressures and partially saturated permeabilities induce water infiltration from top to bottom in aporous medium. As shown in Figure 7(a, b), three locations at the surface (A), middle (B) and bottom (C) of the slope, were selected for observing permeability effects. The solid–fluid transition was initially disabled.

Figure 8(a, b) shows the suction time histories at A, B and C under two different initial saturated permeabilities: $k_s = 1 \cdot 10^{-3}$ m/s and $1 \cdot 10^{-4}$ m/s. The suctions decrease over time because of infiltration at different altitudes. The suction was always smaller at the free surface than at the bottom, because it takes longer for seeping rainwater to reach greater depths. Moreover, the suction in the inferior layers decreased more quickly under a greater permeability, while the variations at the surface were identical. The suction variation at the slope's surface is determined by the same water flux; however, the amount of water infiltrating the ground is partially controlled by the permeability of the partially saturated soil according to Darcy's law.

Table 1. Elasto-plastic parameters.

Property of soil	E	ν	$\varphi_{e0} = \varphi_{c0}$	$\varphi_{ef} = \varphi_{cf}$	c_0	c_f	$\psi_e = \psi_c$	B_p	B_c	ρ	η	s_y
Unit	MPa		°	°	kPa	kPa	°			kg/ m ³	Pa s	kPa
Value	3	.35	15	25	0	0	10	.01	.02	1100	150	5

Table 2. Hydraulic and hydro-mechanical coupling parameters.

Hydraulic parameters					Hydro-mechanical coupling parameters					Permeability k_s
a_d	n_d	a_w	n_w	Sr_{sat}	Sr_{res}	a_χ	n_χ	λ	n_0	$1 \cdot 10^{-3}$ and $1 \cdot 10^{-4}$ m/s
.802	1.38	.802	1.38	1	0	.6805	1.5847	.5	.39	

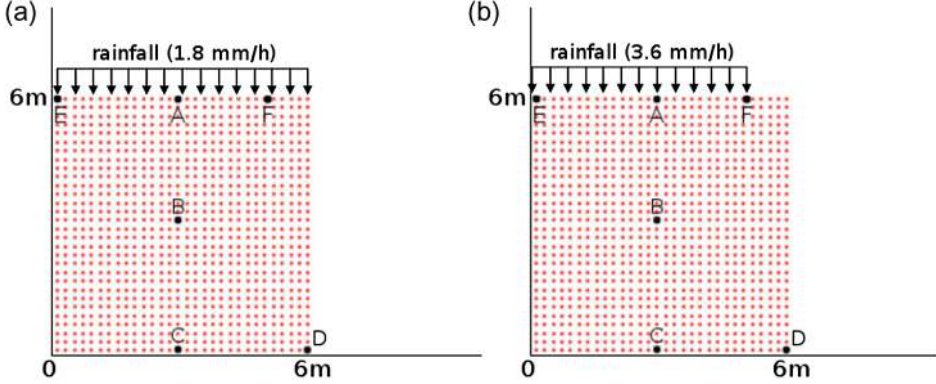


Figure 7 (a, b). Geometry of the column under different hydraulic boundary conditions.

Figure 9(a, b) shows the variations in the partially saturated permeabilities with respect to time. For the higher saturated permeability $k_s = 1 \cdot 10^{-3}$ m/s, the initial partially saturated permeability of $5 \cdot 10^{-7}$ m/s, determined using Equation (27), was nearly equal to the water flux. This suggests that the water permeated almost completely into the slope. However, for the lower saturated permeability $k_s = 1 \cdot 10^{-4}$ m/s, the calculated partially saturated permeability was approximately $6 \cdot 10^{-8}$ m/s, which is notably less than the water flux. Thus, in this case, only a portion of water infiltrated the ground.

4.2. Simulation and analysis of a solid–fluid transition

If a solid–fluid transition is activated, a point of failure can be reached and a mudflow can occur. The entire mudflow process was simulated with a water flux of $1 \cdot 10^{-6}$ m/s (3.6 mm/h) on the 5 m E-F boundary (shown previously in Figure 7(b)). Initial and final effective cohesions were $c'_0 = 0, 10$ and 25 kPa, and $c'_f = 0, 25$ and 45 kPa. Tables 3 and 4 list additional parameters used in this simulation.

Figure 10 shows the delayed failure with increasing effective cohesions attributable to the global second-order work criterion. The increased effective cohesions enhance material strength as follows:

$$\tau = c' + \sigma' \tan \varphi' = (c' + \chi_{st} \sigma \tan \varphi') + \bar{\sigma} \tan \varphi' \quad (28)$$

Note that failure cannot be observed for very large cohesion. The FE tool does not allow for calculation of excessive water pressure; the failure of a clayed soil that has a large cohesion cannot be reached.

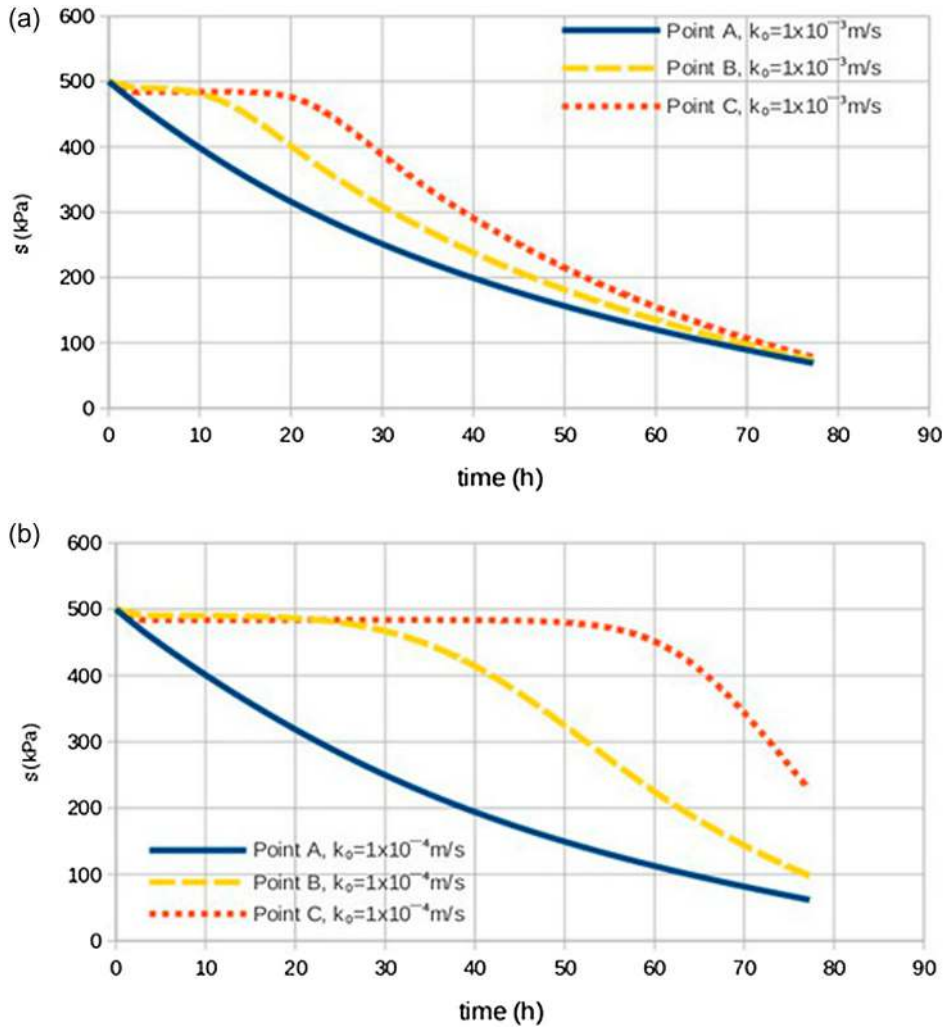


Figure 8. Variations in suctions in the points A, B, and C under the saturated permeability (a) of $1 \cdot 10^{-3}$ m/s and (b) $1 \cdot 10^{-4}$ m/s.

When $c'_0 = 25$ kPa and $c'_f = 45$ kPa, failure occurs after a rainfall episode lasting 46 h, corresponding to the disappearance of the global second-order work (i.e. Bingham's yield stress is exceeded before the elastic limit is reached). Once failure occurs, the flowing geomaterials obey Bingham's viscous law. As detailed by Prime et al., (2013) and (2014), the physical viscosity and yield stress influence the stop time. Considering two different viscosities of $\eta = 150$ and 300 Pa·s, Figure 11 shows the horizontal displacements of D (shown previously in Figure 7(b)) over time. Not surprisingly, higher viscosities induced smaller displacements.

Figure 12(a–f) includes a series of pre-failure suction field images at various points in time ranging from 11 to 46 h, and post-failure mudflow images at 2 and 14 s after failure for a viscosity of $\eta = 150$ Pa·s. Following initial vertical infiltration at the surface E-F, horizontal infiltration was observed, due to the water pressure gradient in the

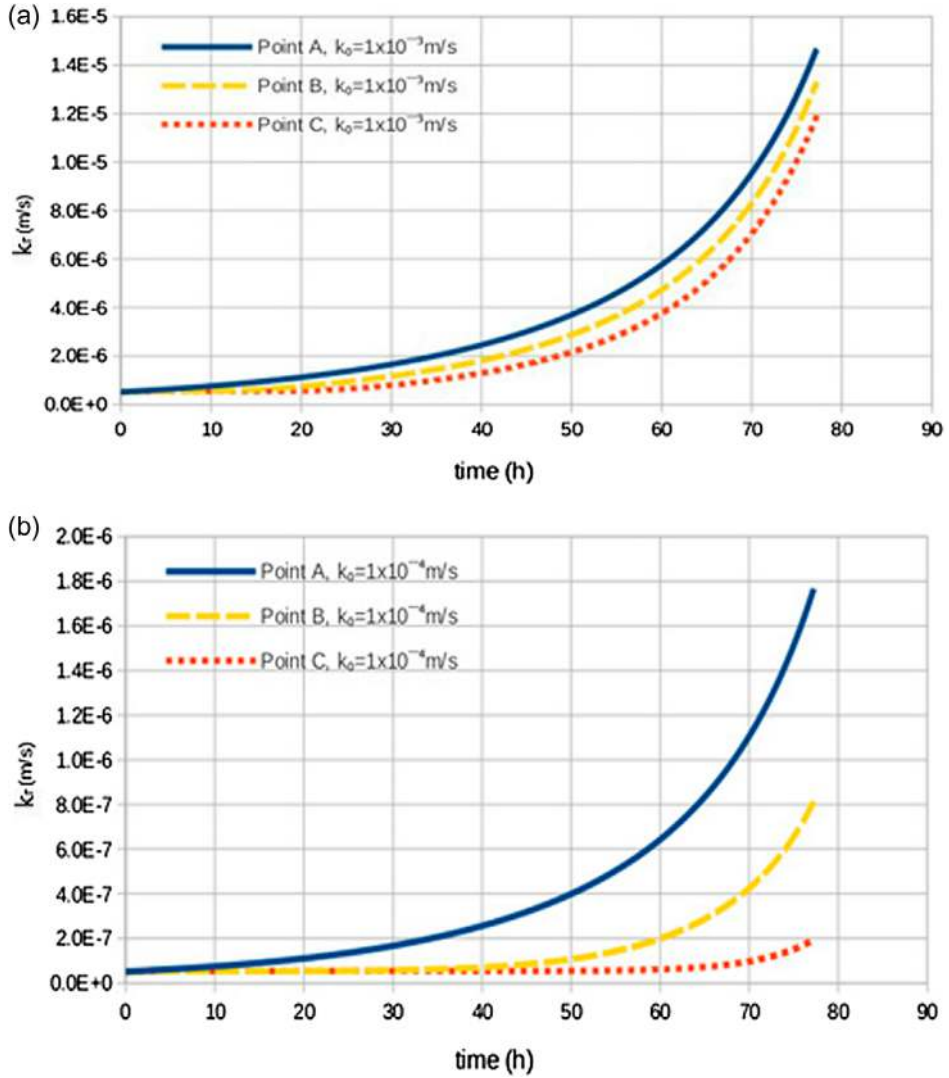


Figure 9. Variations of partially saturated permeabilities in the points A, B, and C under the saturated permeability (a) of $1 \cdot 10^{-3}$ m/s and (b) $1 \cdot 10^{-4}$ m/s.

Table 3. Elasto-plastic parameters.

Property of soil	E	ν	$\varphi_{c0} = \varphi_{c0}$	$\varphi_{ef} = \varphi_{ef}$	$\psi_e = \psi_c$	B_p	B_c	ρ	η	s_y
Unit	MPa		°	°	°			kg/m ³	Pa s	kPa
Value	5	.35	15	25	10	.01	.02	1100	150	12

horizontal direction and horizontal permeability. As shown in Figure 12(f), the yield stress s_y , exceeded the second invariant of stress tensor $J_{2\sigma}$, for the soil particles causing the mudflow to stop.

Table 4. Hydraulic and hydro-mechanical coupling parameters.

Hydraulic parameters						Hydro-mechanical coupling parameters				Permeability k_s
a_d	n_d	a_w	n_w	Sr_{sat}	Sr_{res}	a_χ	n_χ	λ	n_0	$7 \cdot 10^{-5} \text{ m/s}$
.802	1.38	.802	1.38	1	0	.6805	1.5847	.5	.39	

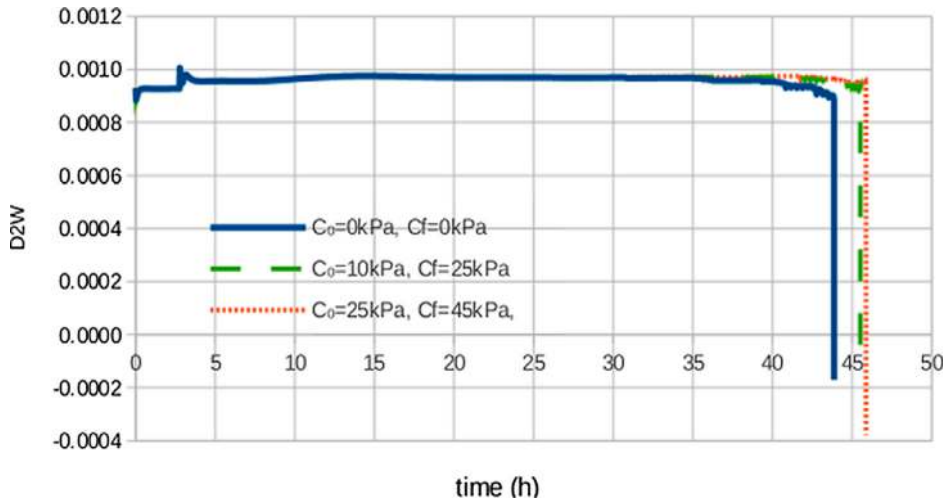


Figure 10. Influence of effective cohesions on the failure.

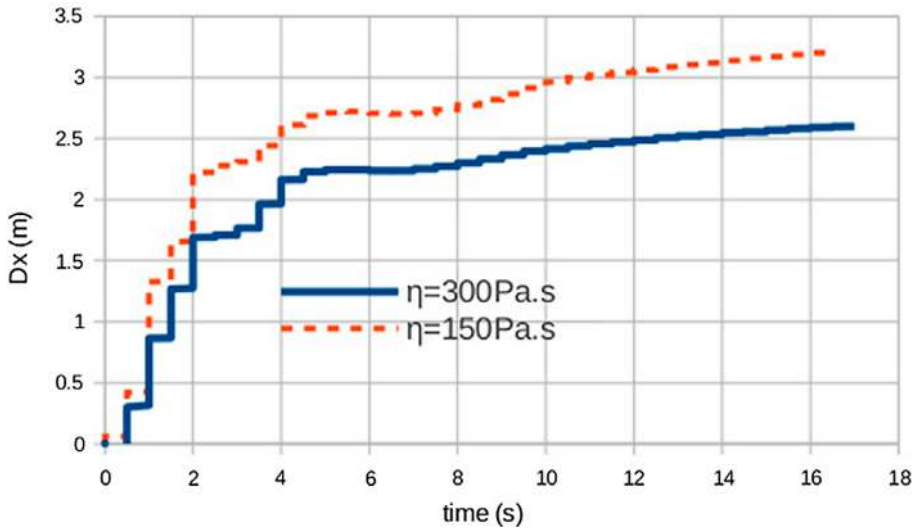


Figure 11. Influence of viscosity coefficient on horizontal displacements.

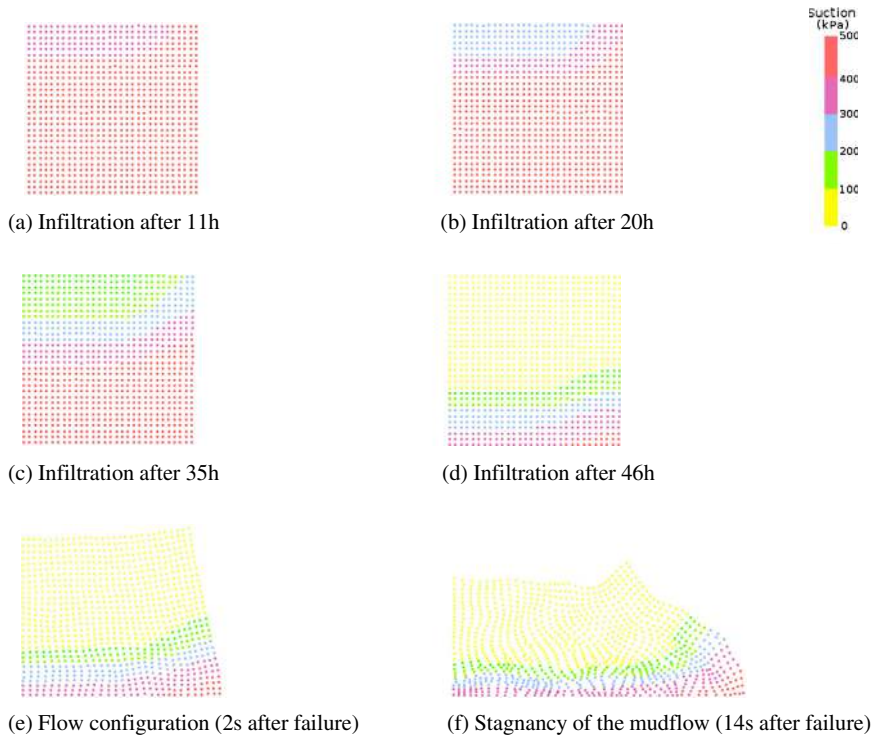


Figure 12. (a–d) Reduction of suctions in different layers during the pre-failure stage; and (e, f) configurations of the mudflow during the post-failure stage.

5. FEMLIP simulation of a real rainfall-induced mudflow

After applying the FEMLIP model to a heuristic partially saturated column, it was next used to simulate a real mudflow that occurred in China. Figure 13 shows the geological profile of the affected slope. The slope is situated in southern China where a subtropical monsoon climate prevails, and precipitation is abundant in June, July and August. Following multiple years of drying–wetting cycles, a large number of fissures emerged. This phenomenon is considered accelerating water entry into the soils. During an intense four-day rainfall, failure occurred on the third day, affecting all layers of the slope including the bottom gravel layer.

5.1. FEMLIP model

According to the geological profile illustrated in Figure 13, a FEMLIP model was built to simulate the observed mudflow. As shown in Figure 14, the model used the inclined boundaries as the bedrock surface. All boundaries were free slip. The length of the slope was 60 m and the height was 30 m. The mesh was formed using quadrilateral bilinear elements: 12 along the z -axis and 60 along the model length, parallel to the boundaries. Gravity increased from 0 to 9.8 m/s in the first 100 time steps ($\Delta t = .1$ s) and remained constant in the subsequent 100 time steps. After 200 time steps, a water flux of 53.8 mm/h, induced by the rainfall, was applied to the surface of the slope until a solid–fluid transition occurred.

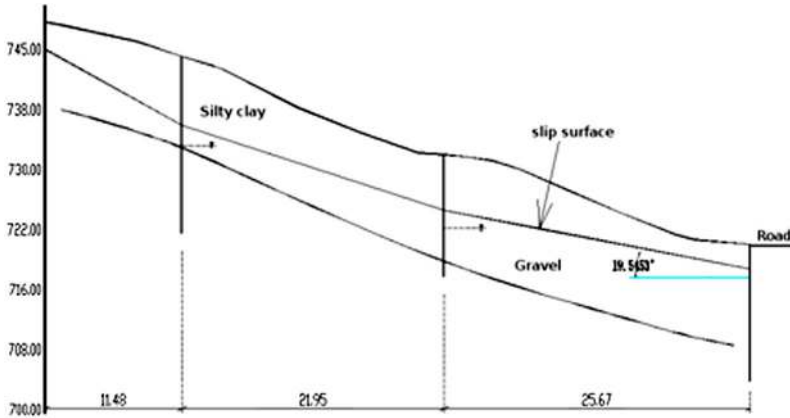


Figure 13. Geological profile of the slope.

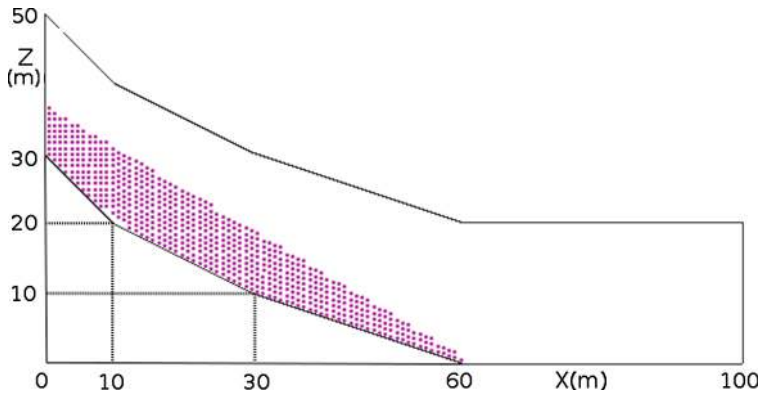


Figure 14. FEMLIP model of the mudflow.

5.2. Physical and mechanical parameters

The unified model with a solid–fluid transition and hydro-mechanical coupling required 13 PLASOL model parameters, 2 Bingham’s law parameters, 4 hydro-mechanical coupling parameters and 7 hydraulic parameters (including a saturated permeability that is assumed isotropic). With dry density and initial suction, 28 total parameters were required. To minimise the number of parameters determined for the elasto-plastic law, $\varphi_c = \varphi_e$ and $\psi_c = \psi_e$ were assumed throughout the calculation. The convexity n was set to -0.229 , and the two hardening parameters B_p and B_c were set to $.01$ and $.02$, respectively (Prunier, 2008). For the hydraulic model, the effect of hysteresis does not intervene the monotonous formation of a mudflow. As illustrated in Figure 15, hysteresis was neglected and the cycle was determined using the two parameters, a_w and n_w ; the infiltration process was considered a monotonous wetting process. These assumptions reduced the number of required parameters from 28 to 20 for each geomaterial: 7 elasto-plastic parameters, 2 viscous parameters, 4 hydro-mechanical coupling parameters, 5 hydraulic parameters, the dry density and the initial suction (or the initial degree of saturation).

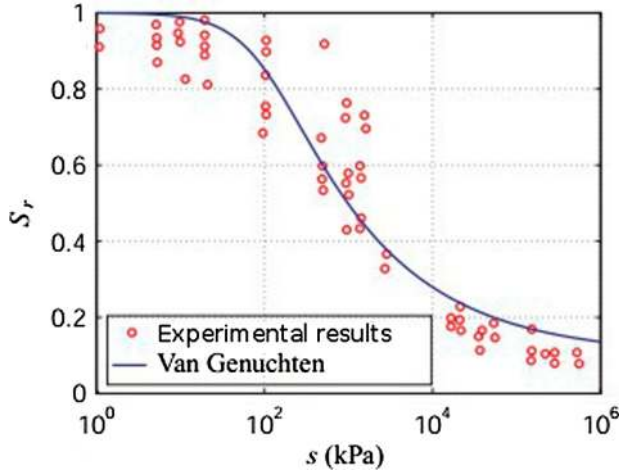


Figure 15. Typical water retention curve of clay (Fleureau et al., 2002).

Values for the elasto-plastic parameters, the initial degree of saturation, the initial partially saturated permeability and the initial porosity were obtained from the geotechnical data in Table 5.

Only values for the initial degree of saturation, the initial porosity and the initial partially saturated permeability were provided in the geotechnical data; however, determination of the WRC required four hydraulic parameters and the hydro-mechanical coupling required three parameters (a_χ , n_χ and λ). In this study, values proposed by Fleureau, Verbrugge, Huergo, Gomez Correia, and Kheirbek-Saoud (2002) for seven of the required parameters were used to describe the silty clay's hydraulic behaviour. Table 6 lists these parameters and their associated values.

Using Equation (9) and the hydraulic parameters mentioned above, we estimated an initial suction of $s = 159$ kPa with $S_r = 78\%$ for the silty clay. The initial partially saturated permeability was estimated using the Equation (27) as $k = 1 \cdot 10^{-7}$ m/s. This estimate was comparable to the values from the geotechnical data in Table 5. Therefore, the parameters in Table 6 were considered acceptable. This study was focused on the

Table 5. Physical parameters of the silty clay proposed from the geotechnical data.

Parameters of silty clay	Symbol	Unit	Value
Natural density	ρ_n	kN/m ³	1836
Dry density	ρ_d	kN/m ³	1391
Initial porosity	n_0		.38
Initial degree of saturation	S_r	%	78
Initial cohesion	c_0	kPa	34.6
Final cohesion	c_f	kPa	92
Initial angle of friction	$\varphi_{e0} = \varphi_{e0}$	°	11
Final angle of friction	$\varphi_{ef} = \varphi_{cf}$	°	31
Angle of dilation	$\psi_e = \psi_c$	°	5
Initial partially saturated permeability	k	cm/s	$7 \cdot 10^{-6}$
Initial Young's modulus	E	MPa	6.4
Poisson's ratio	ν		.35

Table 6. Hydraulic parameters and parameters of hydro-mechanical coupling.

Hydraulic parameters	Symbol	Value
First parameter of water-retention curves	a_w	1
Second parameter of water-retention curves	n_w	1.35
Saturated degree of saturation	$S_{r_{sat}}$	1
Residual degree of saturation	$S_{r_{res}}$.1
<i>Parameters of hydro-mechanical coupling</i>		
First parameter of χ	a_χ	2
Second parameter of χ	n_χ	2.15
	λ	.5

hydro-mechanical coupling in a solid state. The viscous parameters were heuristically chosen as $\eta = 220$ Pa s, and $s_y = 16$ kPa, for the post-failure flow simulation.

6. Results

Figure 16(a, b) shows the increased gravity over time, and the evolution of the global second-order work, D^2W with respect to gravity in first 200 time steps. The D^2W represented in Figure 16(b) decreased but remained positive. Obviously, the initialisation of gravity did not induce any instability.

Figure 17 shows the evolution of the D^2W under rainfall infiltration. In this case, the D^2W was positive and relatively constant at the beginning of infiltration. After approximately 21 h of rainfall, the D^2W gradually decreased and eventually assumed a negative value after more than two days of rainfall (approximately 52 h, as observed in the real case).

Once the failure occurred, the geomaterial exhibited a fluid-like behaviour and began to flow. Figures 18 and 19 show water infiltration in the soil (decreased suction) and the entire mudflow process, respectively, for various elapsed times. In Figure 19, unstable zones (shown in green) initially appear near the top and toe of the slope. The initial slope suction was homogeneous, but the water pressure gradient in these zones was larger than the gradient on the surface under identical hydraulic conditions (i.e. a water flux of 53.8 mm/h). This phenomenon accelerated the water infiltration and the decrease in suction. Figure 18 confirms that the suctions in the unstable zones decreased more rapidly.

Over time, unstable zones appeared on the surface of the slope. Higher suctions in the top layer reduced cohesion. Unstable zones subsequently spread along the bedrock, producing a failure zone in the steepest slope.

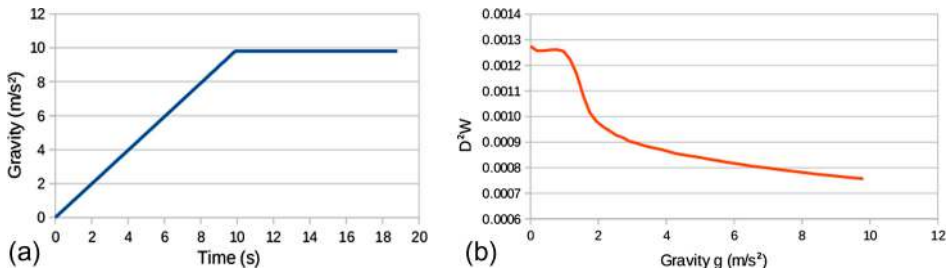


Figure 16. (a) Initialisation of the gravity with time, and (b) variation of the global second-order work. D^2W in the initialisation phase.

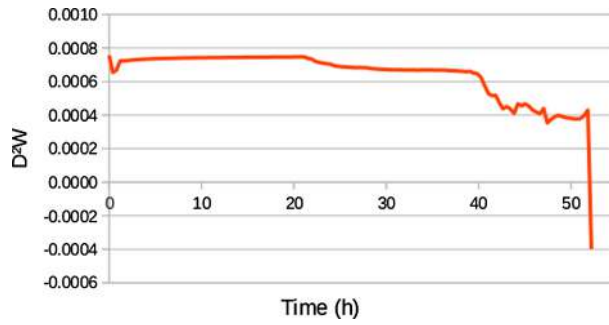


Figure 17. Evolution of the global second-order work with the rainfall infiltration before the failure.

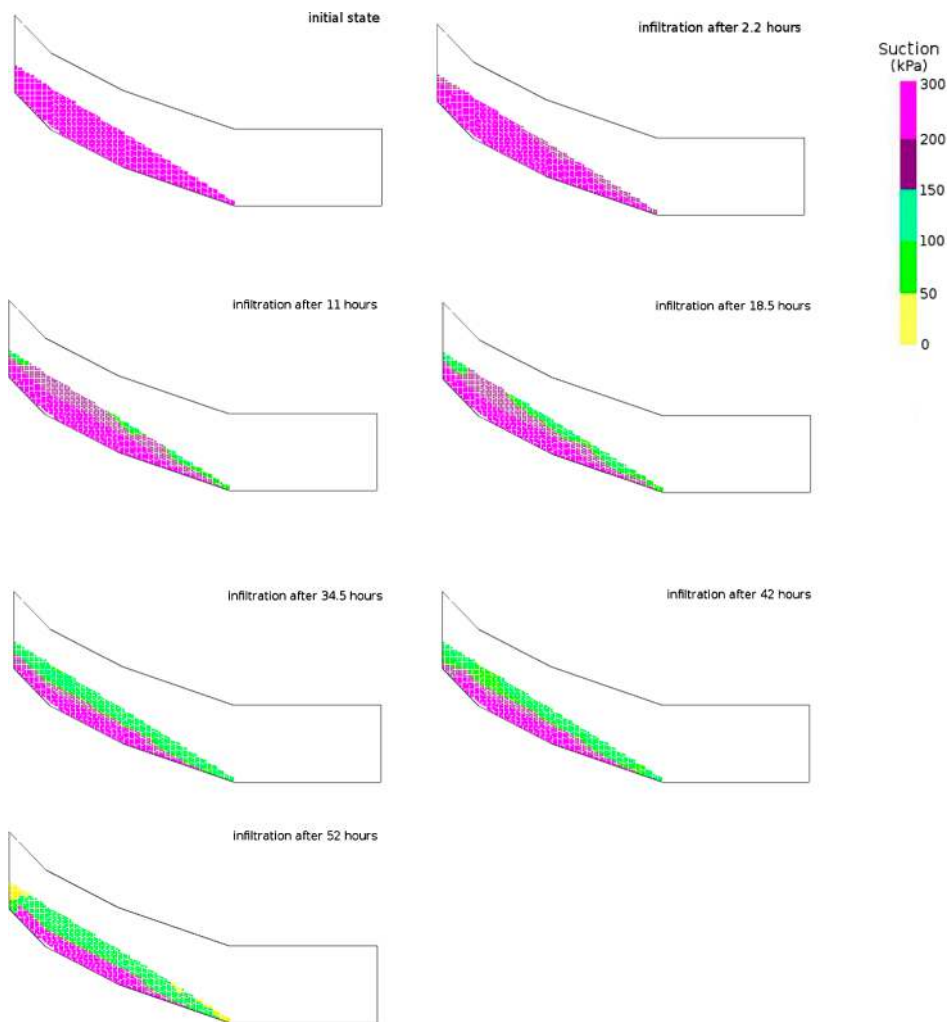


Figure 18. Evolution of the suction field.

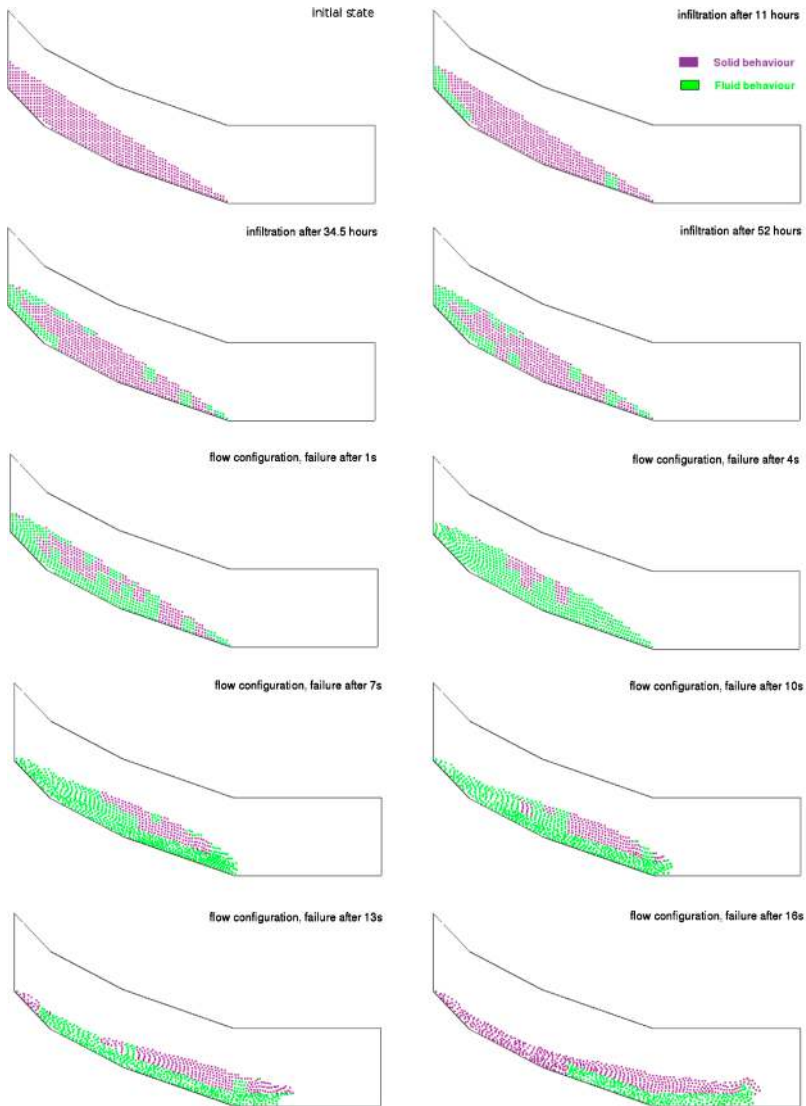


Figure 19. Evolution of the unstable zones and the flow configurations.

When the global second-order work became negative, the slope was globally unstable. The soil slipped along the surface of the bedrock, obeying Bingham's law. At the end of the simulation, the yield stress s_y exceeded the second invariant of stress tensor $J_{2\sigma}$ for the soil particles and the mudflow stops.

7. Conclusions

Within the framework of a unified hydro-elasto-plastic model with a solid–fluid transition (Li et al., 2016), a new FEM-LIP formulation for modelling landslides or mudflows was proposed in this study. The proposed FEM-LIP model includes the following assumptions:

(1) liquid and solid phases are incompressible; (2) heat transfer is negligible and the temperature field is assumed constant; (3) generalised Darcy's law can be used to describe the liquid flowing in the connected voids of the medium; and (4) air pressure and water vapour pressure are nil under atmospheric air pressure. This study additionally implemented a new solver based on the BiCGSTAB for inverting non-symmetric matrices.

To evaluate the proposed FEMLIP model, a heuristic partially saturated column with a homogeneous initial suction and water flux at the top boundary were initially simulated. Permeability effects of partially saturated soil due to infiltration were assessed. Water mass conservation effects were observed, and the role of effective cohesion in failure (due to apparent cohesion variation as stated in Equation (28)) was demonstrated. Subsequently, a real rainfall-induced mudflow was simulated. The failure induced by infiltration was observed after 52 h when the global second-order work vanished. This simulated finding was consistent with observed findings from the real mudflow. An entire mudflow process was illustrated by analysing the evolution of the suction field and development of unstable zones. Based on this study's results, the proposed FEMLIP model appears to be effective in describing behaviours of partially saturated soil, in both solid and fluid regimes.

In case of sudden failure, inertial effects can influence the computation of the velocity field, especially during the beginning and end of landslides. The inertial force can be considered explicitly as a supplemental nodal force, or implicitly by introducing it into the stiffness matrix.

This study investigated the initiation and propagation of a landslide in a unified framework. The elasto-plastic constitutive parameters and Bingham's viscous parameters characterise the same material, but in different states. It is reasonable to assume a correlation between the two sets of parameters. However, the lack of reliable experimental data from international literatures limits further investigation of the correlations. Further experimentations with mudflow material in both pre-failure and post-failure states would support determination of any elasto-plastic and viscous parameter correlations. In addition, such experimentation may reveal additional correlations. For example, viscosity is also dependent on the fine content of soil.

Acknowledgements

The 3SR Laboratory is part of LabEx Tec 21.

Disclosure statement

No potential conflict of interest was reported by the authors.

Funding

This work was supported by the China Scholarship Council.

References

- Abe, K., Soga, K., & Bandara, S. (2014). Material point method for coupled hydromechanical problems. *Journal of Geotechnical and Geoenvironmental Engineering*, 140, 04013033 1–15.
- Alonso, E. E., Gens, A., & Delahaye, C. (2003). Influence of rainfall on the deformation and stability of a slope in overconsolidated clays: A case study. *Hydrogeology Journal*, 11, 174–192.

- Alonso, E. E., Pereira, J. M., Vaunat, J., & Olivella, S. (2010). A microstructurally based effective stress for unsaturated soils. *Géotechnique*, *60*, 913–925.
- Arairo, W., Prunier, F., Djéran-Maigre, I., & Darve, F. (2013). A new insight into modelling the behaviour of unsaturated soils. *International Journal for Numerical and Analytical Methods in Geomechanics*, *37*, 2629–2654.
- Au, S. W. C. (1998). Rain-induced slope instability in Hong Kong. *Engineering Geology*, *51*, 1–36.
- Balmforth, N. J., & Craster, R. V. (1999). A consistent thin layer theory for Bingham plastics. *Journal of Non-Newtonian Fluid Mechanics*, *84*, 65–81.
- Bandara, S., Ferrari, A., & Laloui, L. (2016). Modelling landslides in unsaturated slopes subjected to rainfall infiltration using material point method. *International Journal for Numerical and Analytical Methods in Geomechanics*, *40*, 1358–1380.
- Bardenhagen, S. G., & Kober, E. M. (2004). The generalized interpolation material point method. *Computer Modeling in Engineering and Sciences*, *5*, 477–495.
- Barnichon, J. D. (1998). *Finite element modelling in structural and petroleum geology* (Ph.D. Thesis). University of Liege, Liege.
- Beuth, L., Wiecekowsky, Z., & Vermeer, P. A. (2011). Solution of quasi-static large-strain problems by the material point method. *International Journal for Numerical and Analytical Methods in Geomechanics*, *35*, 1451–1465.
- Bishop, A. W. (1959). Principle of effective stress. *Teknisk Ukeblad*, *106*, 859–863.
- Cascini, L., Cuomo, S., Pastor, M., Sorbino, G., & Piciullo, L. (2014). SPH run-out modelling of channelised landslides of the flow type. *Geomorphology*, *214*, 502–513.
- Chen, H., Dadson, S., & Chi, Y. (2006). Recent rainfall-induced landslides and debris flow in northern Taiwan. *Geomorphology*, *77*, 112–125.
- Coussot, P., Proust, S., & Ancey, C. (1996). Rheological interpretation of deposits of yield stress fluids. *Journal of Non-Newtonian Fluid Mechanics*, *66*, 55–70.
- Daido, A. (1971). On the occurrence of mud-debris flow. *Bulletin of the Disaster Prevention Research Institute, Kyoto University*, *21*, 109–135.
- Darve, F., Servant, G., Laouafa, F., & Khoa, H. D. V. (2004). Failure in geomaterials: Continuous and discrete analyses. *Computer Methods in Applied Mechanics and Engineering*, *193*, 3057–3085.
- Dufour, F. (2002). *Développements de la méthode des éléments finis avec des points d'intégration Lagrangiens: Applications à la géomécanique* [Developments of the finite element method with Lagrangian integration points: application in the geomechanics] (Ph.D. Thesis). Ecole centrale de Nantes, Nante.
- Dufour, F., & Pijaudier-Cabot, G. (2005). Numerical modelling of concrete flow: homogeneous approach. *International Journal for Numerical and Analytical Methods in Geomechanics*, *29*, 395–416.
- Duvaut, G., & Lions, J. L. (1972). Transfert de Chaleur Dans un fluide de Bingham dont la viscosité dépend de la température [Heat transfer in a Bingham's fluid whose viscosity depends on the temperature]. *Journal of Functional Analysis*, *11*, 93–110.
- Feng, M., & Fredlund, D. G. (1999). Hysteretic influence associated with thermal conductivity sensor measurements. *Proceedings from Theory to the Practice of Unsaturated Soil Mechanics in Association with the 52nd Canadian Geotechnical Conference and the Unsaturated Soil Group, Regina, Sask*, *14*, 14–20.
- Fleureau, J. M., Verbrugge, J.-C., Huergo, P. J., Gomez Correia, A., & Kheirbek-Saoud, S. (2002). Aspects of the behaviour of compacted clayey soils on drying and wetting paths. *Canadian Geotechnical Journal*, *39*, 1341–1357.
- Fredlund, D. G., & Xing, A. (1994). Equations for the soil-water characteristic curve. *Canadian Geotechnical Journal*, *31*, 521–532.
- Gallipoli, D., Gens, A., Sharma, R., & Vaunat, J. (2003). An elasto-plastic model for unsaturated soil incorporating the effects of suction and degree of saturation on mechanical behaviour. *Géotechnique*, *53*, 123–135.
- Harlow, F. H. (1964). The particle-in-cell computing method for fluid dynamics. *Computer Methods in Physics*, *3*, 319–343.
- Hughes, T. J. R. (1987). *The finite element method*. Englewood Cliffs, NJ: Prentice-Hall Inc.

- Khoa, H. D. V. (2005). *Modélisation des glissements de terrain comme un problème de bifurcation* [Modelling landslides as a bifurcation problem] (Ph.D. Thesis). Institut National Polytechnique de Grenoble, Grenoble.
- Khoa, H. D. V., Georgopoulos, I. O., Darve, F., & Laouafa, F. (2006). Diffuse failure in geomaterials. *Computers and Geotechnics*, 33, 7–14.
- Laouafa, F., Prunier, F., Daouadji, A., Al Gali, H., & Darve, F. (2011). Stability in geomechanics, experimental and numerical analyses. *International Journal for Numerical and Analytical Methods in Geomechanics*, 35, 112–139.
- Li, Z. H., Dufour, F., & Darve, F. (2016). Hydro-elasto-plastic modelling with a solid/fluid transition. *Computers and Geotechnics*, 75, 69–79.
- Moresi, L. N., & Solomatov, V. S. (1995). Numerical investigation of 2D convection with extremely large viscosity variations. *Physics of Fluids*, 7, 2154–2162.
- Moresi, L., Dufour, F., & Mühlhaus, H.-B. (2002). Mantle convection modeling with viscoelastic/brittle lithosphere: Numerical methodology and plate tectonic modeling. *Pure and Applied Geophysics*, 159, 2335–2356.
- Moresi, L., Dufour, F., & Mühlhaus, H.-B. (2003). A Lagrangian integration point finite element method for large deformation modeling of viscoelastic geomaterials. *Journal of Computational Physics*, 184, 476–497.
- Mualem, Y. (1974). A conceptual model of hysteresis. *Water Resources Research*, 10, 514–520.
- Nakata, Y., Liu, D., Hyodo, M., Yoshimoto, N., & Kato, Y. (2010). Numerical simulation of an expressway embankment slope failure. *Unsaturated Soil: Theoretical and Numerical Advances in Unsaturated Soil Mechanics*. Newcastle, Australia, 719–724.
- Nicot, F., Dauadji, A., Laouafa, F., & Darve, F. (2010). Second-order work, kinetic energy and diffuse failure in granular materials. *Granular Matter*, 13, 19–28.
- Parlange, J.-Y. (1980). Water Transport in Soils. *Annual Review of Fluid Mechanics*, 12, 77–102.
- Pastor, M., Blanc, T., Haddad, B., Drempevic, V., Morles, M. S., Dutto P., ... Fernandez Merodo, J. A. (2015). Depth averaged models for fast landslide propagation: Mathematical, rheological and numerical aspects. *Archives of Computational Methods in Engineering*, 22, 67–104.
- Petley, D. (2012). Global patterns of loss of life from landslides. *Geology*, 40, 927–930.
- Prime, N. (2012). *Modélisation de la transition solide-fluide dans les géomatériaux. Application aux glissements de terrain* [Modelling the solid-fluid transition in geomaterials. Application in landslides] (Ph.D. Thesis). Institut National Polytechnique de Grenoble, Grenoble.
- Prime, N., Dufour, F., & Darve, F. (2013). Unified model for geomaterial solid/fluid states and the transition in between. *Journal of Engineering Mechanics*, 140, 682–694.
- Prime, N., Dufour, F., & Darve, F. (2014). Solid-fluid transition modelling in geomaterials and application to a mudflow interacting with an obstacle. *International Journal for Numerical and Analytical Methods in Geomechanics*, 38, 1341–1361.
- Prunier, F. (2008). *Modélisation des instabilités en géomécanique, application aux glissements de terrain* [Modelling instabilities in geomechanics, application in the landslides] (Ph.D. Thesis). Institut National Polytechnique de Grenoble, Grenoble.
- Prunier, F., Laouafa, F., Lignon, S., & Darve, F. (2009). Bifurcation modeling in geomaterials: From the second-order work criterion to spectral analyses. *International Journal for Numerical and Analytical Methods in Geomechanics*, 33, 1169–1202.
- Scholtès, L., Hicher, P.-Y., Nicot, F., Chareyre, B., & Darve, F. (2009). On the capillary stress tensor in wet granular materials. *International Journal for Numerical and Analytical Methods in Geomechanics*, 33(10), 1289–1313.
- Scholtès, L., Chareyre, B., Nicot, F., & Darve, F. (2009). Micromechanics of granular materials with capillary effects. *International Journal of Engineering Science*, 47, 64–75.
- Sheng, D., Sloan, S. W., & Gens, A. (2004). A constitutive model for unsaturated soils: Thermomechanical and computational aspects. *Computational Mechanics*, 33, 453–465.
- Soga, A., Alonso, E., Yerro, A., Kumar, K., & Bandara, S. (2015). Trends in large deformation analysis of landslide mass movement. *Géotechnique*, 00, 1–23.
- Taylor, D. (1948). *Fundamentals of soil mechanics*. London: Wiley.
- van der Vorst H. A. (1992). Bi-CGSTAB: A fast and smoothly converging variant of bi-cg for the solution of nonsymmetric linear systems. *SIAM Journal on Scientific and Statistical Computing*, 13, 631–644.

- Van Eekelen, H. A. M. (1980). Isotropic yield surface in three dimensions for use in soil mechanics. *International Journal for Numerical and Analytical Methods in Geomechanics*, 4, 89–101.
- Van Genuchten, M. T. (1980). A closed-form equation for predicting the hydraulic conductivity of unsaturated soils. *Soil Science Society of America Journal*, 44, 892–898.
- Wheeler, S. J., Sharma, R. J., & Buisson, M. S. R. (2003). Coupling of hydraulic hysteresis and stress–strain behaviour in unsaturated soils. *Géotechnique*, 53(1), 41–54.
- Zhang, X., Krabbenhoft, K., Sheng, D., & Li, W. (2015). Numerical simulation of a flow-like landslide using the particle finite element method. *Computational Mechanics*, 55, 167–177.